Available on CMS information server

CMS NOTE-2008/017

The Compact Muon Solenoid Experiment

CMS Note

Mailing address: CMS CERN, CH-1211 GENEVA 23, Switzerland

18 October 2007

CMS DT Chambers: Optimized Measurement of Cosmic Rays Crossing Time in absence of Magnetic Field

M. Benettoni, F. Gasparini, F. Gonella, A. Meneguzzo, S. Vanini, G. Zumerle

University of Padova and INFN Padova, Italy

G. Bonomi

University of Brescia and INFN Pavia, Italy

Abstract

Two spare drift chambers produced in the I.N.F.N. Legnaro Laboratory (Padova, Italy) for the barrel muon spectrometer of the LHC CMS experiment have been extensively tested using cosmic-ray muons. A fitting algorithm was developed to optimize the determination of the time of passage of the particle. A timing resolution of $\approx$2 ns has been obtained. The algorithm permits the measurement of the track reconstruction precision of the chambers by using cosmic-ray data with the same accuracy obtained using high-energy test-beam data.

1 Introduction

Two spare muon drift tube (DT) chambers of the MB3 type have been used in the I.N.F.N. Laboratory in Legnaro, Padova (LNL) to assess the feasibility and limits of what is called muon tomography. This technique uses the multiple scattering of cosmic muons to infer the density of materials contained in closed volumes. The CMS DT chambers were placed above and below the volume to detect crossing muons.

A key requirement of the project is the accurate reconstruction of the muon trajectories before and after crossing the volume under analysis. To this purpose a new fitting procedure of muon tracks has been developed with the aim of optimizing time and space resolution in absence of external timing devices. This procedure can improve the muon track reconstruction and the time of flight measurement in CMS, at least in those zones of the chambers where the residual magnetic field is negligible.

The goal of the paper is to present this fitting procedure and the results obtained concerning space and time resolution.

2 CMS Detector DT Chambers

The main component of the CMS barrel muon detection system [1] consists of 4 concentric shells of wire drift chambers called, moving outward, MB1, MB2, MB3, and MB4. They are located on 4 concentric layers around the beam line inside the 5 wheels of the iron yoke of the CMS barrel. MB3 chambers were produced in LNL during the years 2001–2005.

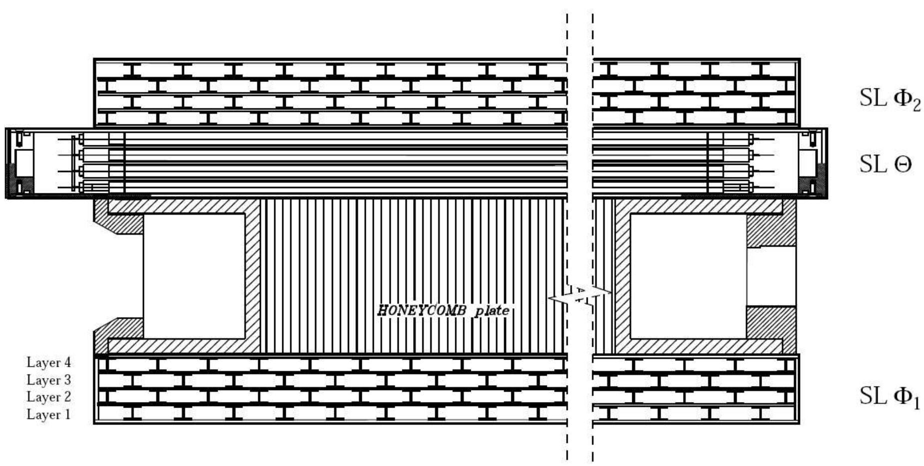

Figure 1: MB chamber cross section.

2.1 CMS Drift Tube Chamber Layout

Each CMS DT muon chamber [2] consists of 3 independent units, called "Super Layers" (SL), attached to a structural honeycomb support (Fig. 1). Each SL is composed of 4 planes of parallel rectangular drift tubes called "layers". Each layer is staggered by a half cell with respect to the contiguous ones. Two SLs, named $SL_{\Phi 1}$ and $SL_{\Phi 2}$, have wires in the same direction. In CMS they measure the muon track position and direction in the bending plane (ρ–ϕ plane in the CMS coordinate system). The third SL, named SL_{Θ}, has perpendicular wires and measures the track coordinate parallel to the beam direction.

The cross section of a drift tube is shown schematically in Figure 2. The pitch between 2 adjacent cells in a layer is 42 mm, while the distance between the wire planes of 2 consecutive layers is 13 mm. The electric field in the drift cell is shaped as follows: a wire, kept at positive voltage, where the electron multiplication occurs; 2 cathodes at negative voltage; and 2 central strip electrodes with intermediate voltage between wire and ground, whose purpose is to improve field uniformity along the drift path. The MB3 chamber wire length is 237.9 cm and 302.1 cm for SL_{Φ} and SL_{Θ}, respectively. Each SL_{Φ} contains 286 channels, while the SL_{Θ} contains 227 channels, for a total of 799 channels per chamber. Any charged particle going through a cell volume will generate a signal in its anode

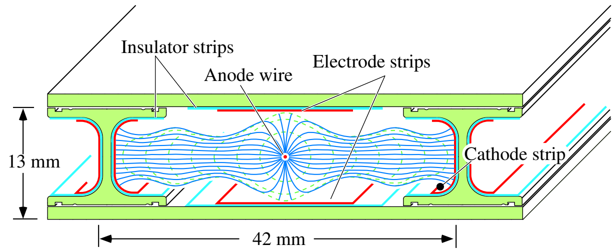

Figure 2: Schematic view of a drift tube. The drift lines (continuous lines) and the isochronous surfaces (dotted lines), computed with the CERN program GARFIELD [3], are also shown.

wire.

The wire signal is processed by the front-end electronics (FE) [4], composed of a fast charge preamplifier (33 ns integration time) followed by a shaper (shaping time 15 ns) and a discriminator. Signals from the front-end electronics are fed into the so-called MiniCrate, an aluminum structure attached to the chambers honeycomb, which hosts the DT trigger electronics (Trigger Boards; TRB) and the Read-Out Boards (ROB) [6], together with the necessary services.

The trigger electronics located in the MiniCrate delivers a trigger signal at a fixed time after the passage of a particle. Details about the trigger electronics can be found in [5]. The core of the system is a custom VLSI, called the "Bunch and Track Identifier" (BTI). Each BTI reads 9 adjacent wire signals in a single SL, and reconstructs the signals alignment from the 4 layers of the SL. The alignment is checked by a sophisticated algorithm called the generalized mean-timer method, interpreted roughly as a line fit. An additional device named the "Track Correlator" (TRACO) looks for alignment of the track segments of the 2 SL_Φ. The number of aligned hits (3 or 4) in the SL segments and the correlation between the segments of the 2 SL_Φ are used to define a quality flag of the trigger. A third device in the chamber trigger chain, the "Trigger Server" (TS), selects the 2 best quality tracks in the whole chamber. The system has been designed for LHC usage, where particles are bunched at the 40 MHz accelerator frequency, therefore the trigger algorithm output is clocked at the same frequency.

ROBs are built around a 32-channel high performance TDC, developed by the CERN/EP Microelectronics group. The most relevant feature of the TDC is the common-stop mode usage. The stop signal is given by the trigger, and all the wire signals received backwards in time from the stop in a fixed time window (in this case, 3.2 μs) are read from the TDC buffers (counting unit is equal to 25/32 ns). The signal propagation time from FE to ROBs could be different for different channels (the difference is of the order of few nanoseconds), due to the cable lengths inside the MiniCrate. A common test pulse signal can be injected into each FE amplifier channel, and the TDC measurement of the test pulse arriving time is used to correct the TDC output of each channel before data analysis. After this correction, the TDC output value for the channel is the elapsed time from the TDC time origin to the time at which the wire signal reaches the FE.

In standard operating conditions the electrons drift velocity in the cell has approximately a constant value along the full drift path. For this reason the TDC raw time histogram (Fig. 3) has a box-like shape (commonly called a "time-box") when the cells are uniformly illuminated. The box width, representing the maximum drift time in the cell, is about 400 ns. The tail on the right is due to secondary electrons extracted from the cell walls from UV photons generated by the initial avalanche [7].

2.2 Experimental Setup

In the present study, 2 MB3 chambers (MB3-061 and MB3-054) were placed horizontally on a dedicated cosmic-ray stand in LNL. The distance between the chamber was about 50 cm between the chambers middle planes. The 2 chambers were positioned with the wires parallel within about 0.5 mrad. In this way the angles measured in the Φ and Θ views of the 2 chambers could be directly compared without offline alignment corrections.

The cosmic-ray rate through a chamber was about 800 Hz. Cosmic-ray data were collected with the chambers operating with the standard CMS gas-mixture. They were filled with an Ar(85%)–CO_2(15%) gas mixture, kept at atmospheric pressure (typically $p = 1020$ mbar), with a gas flow of 0.2 l/min, roughly corresponding to 1 gas volume exchange every 3 days. The high voltage values of the cell electrodes were $V_{wire} = 3700$ V, $V_{strip} = 1800$ V, and $V_{cathode} = -1200$ V. At these voltages, and with the gas mixture quoted above, the drift velocity has

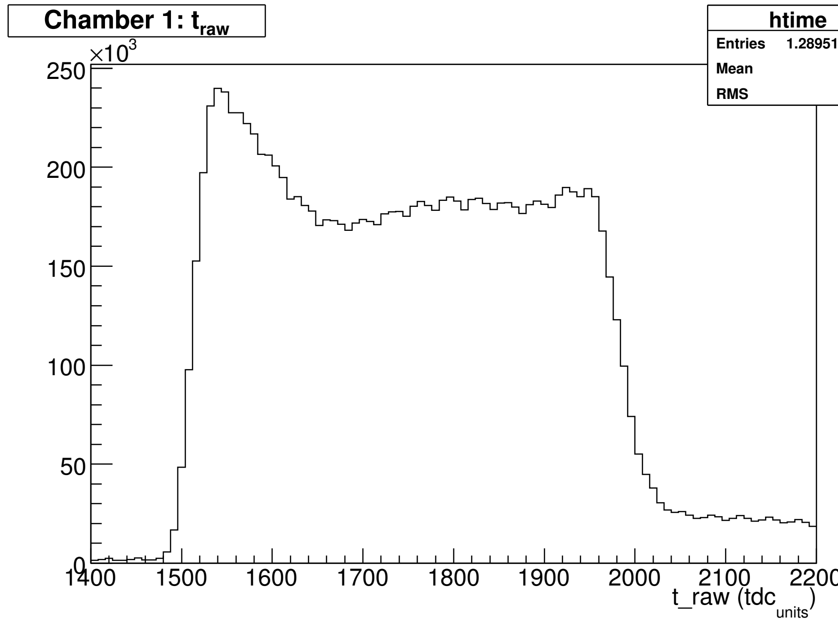

Figure 3: Example of cosmic ray TDC raw time histogram.

the approximately constant value of $v_D \approx 55$ μm/ns along the full drift path [2].

The system operated with the trigger issued by the chamber trigger electronics (autotrigger mode).

3 DT Chamber: Local Track Reconstruction

As pointed out in the introduction, an optimal muon track reconstruction is a key requirement of the muon tomography project. To measure the particle trajectory, the measured points are fitted with a straight line in both views, each chamber separately. In this section we will explain the fit procedure we developed to estimate the track parameters.

3.1 Data Sample and Selection

The results of this note refer to the analysis of a sample of about a million cosmic-ray tracks. Only events where a single track could be identified in both chamber views were considered for the analysis. Events were retained for the analysis if $|\tan(\Phi)| < 0.8$ and $|\tan(\Theta)| < 0.8$. Figure 4 shows the distribution in angle and position of the selected events before the angle acceptance cuts.

Bias from δ rays was reduced by rejecting hits with a too large straight line fit residual (the residual being the difference between the hit coordinate and the coordinate from the line fit). The fit was iterated, discarding at each loop the point whose residual from the fitted line was greater than the usual 3σ. The value of σ, for reasons that will be discussed in Section 4.2.2, was chosen to be a function of the track angle α in the plane perpendicular to the wire as σ = $\left(250 + 200 \cdot \alpha^2\right)$ μm. The iteration was stopped when all the remaining points lay inside the cut. Events for which fewer than 6 points are left in the SL_Φs, or less than 3 in the SL_Θ, were discarded.

3.2 Detection of Cosmic Rays

In the following we will explain in detail the source of the uncertainty in determining the muon crossing time, when cosmic rays are detected with CMS muon chambers. A detailed treatment is necessary, at this point, to understand the relationship between the time value measured by the TDCs (2.1), and the time of passage of the particle through the chamber.

During LHC operation, particles are produced in CMS in collisions bunched in time at the same frequency of the clock used in the trigger circuitry. The Level 1 trigger signal is issued after a fixed number of clock cycles

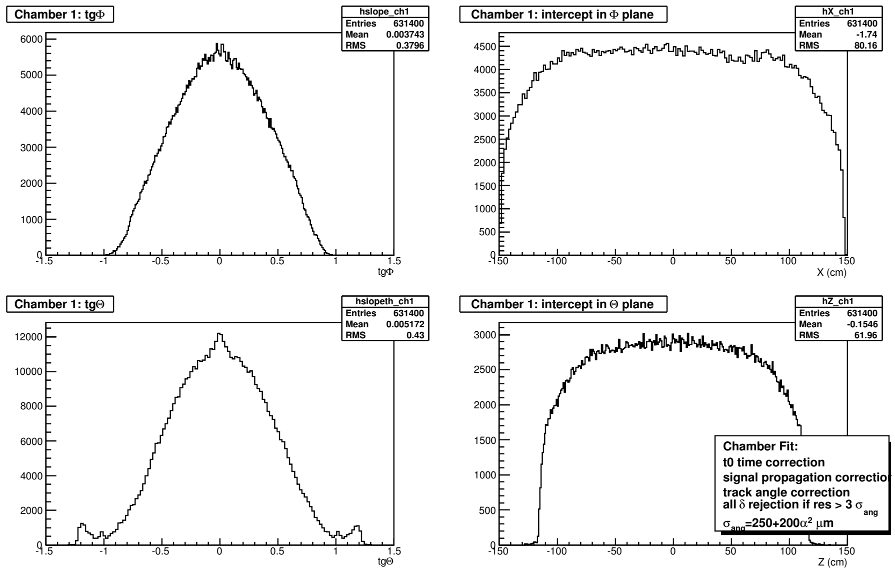

Figure 4: Slope and intercept distributions in Φ and Θ views.

following the clock in which the passage of the particle has happened. The TDC time origin in turn is located a fixed number of clock cycles before the Level 1 trigger signal. Therefore there is a fixed number of clock cycles between the TDC time origin and the clock edge immediately preceding the particle passage. Let's call t_{trig} the time of this clock edge, t_μ the time of passage of the muon, and t_0 the difference between them: $t_0 = t_\mu - t_{trig}$, so that $t_\mu = t_{trig} + t_0$.

The quantity t_{trig} is the same for all the tracks and its value with respect to the TDC time origin can be determined from the known behaviour of the trigger electronics. Alternatively it can be measured from the time box distribution, given a statistically relevant data sample of cosmic events. This second method automatically takes into account the effects of the transit time of signals through cabling and trigger circuitry. Consider muons passing through the wire of a cell. For them the charge amplification occurs without appreciable delay with respect to the particle passage time and the time at which their signal arrives to the FE is practically t_μ. Since the signal transit time from FE to ROB is corrected using the test pulse information, for these muons the TDC value is equal to $t_\mu = t_{trig} + t_0$. All the other muons that hit the chamber far from the wires will have TDC values bigger than this because their signals will be delayed by the drift time of ionization electrons. Therefore, from the time box histogram, t_{trig} is the smallest of all the measured times, the point at which the time box histogram starts.

As concerns the t_0 of LHC events, there is a fixed phase relation between the time at which all the muons leave the interaction point and the clock signal. Therefore the value of t_0 is fixed, and it is calculable using the time of flight of the muon from the interaction point to the chamber. The time t_μ at which the muon crosses a chamber is exactly known for each muon. This is not true for cosmic rays: they arrive randomly distributed in time. For them, t_0 is randomly distributed in the range 0–25 ns and is different from track to track, therefore is not directly calculable. Let's estimate the uncertainty given by the t_0. The drift time of ionization electrons, $t_{drift,i} = t_{TDC,i} - t_\mu$ for cell i, allows to measure the track crossing point. Using the trigger information alone, the best approximation of t_μ is $t_\mu = t_{trig} + 12.5$ ns. This estimate of drift time suffers from the t_0 intrinsic uncertainty. The r.m.s. of the t_0 distribution is $25/\sqrt{12} = 7.2$ ns, corresponding to a position error of ≈400 μm on each layer measurement, completely correlated among the layers. This value has to be compared to the intrinsic resolution of the drift cell, known from test beam measurements to be of the order of 200 μm [11].

The timing error has negative effects on the track parameters determination precision, therefore the distribution of residuals from the fitted trajectory is broader. Two consequences follow:

1. The broader the distribution, the less efficient will be the δ ray cleaning cut. A muon track crossing the chamber layers can produce a δ ray with enough energy to generate ionization electrons far from the muon trajectory. If those electrons are closer to the wire than the muon track, they will produce a signal masking the muon track signal. The measured drift time will be shorter than it should be. The probability for this to

happen is ≈5% per layer [7]. A fraction of these wrong-measured hits can be eliminated with a cut on the tails of the distribution of the residuals.

2. A considerable fraction of the cosmic muons has so low a momentum that the trajectory through the chamber is affected by multiple scattering in a sizeable way. As a consequence, the chamber space precision appears to be worse with cosmic rays than with high-energy particles. In principle, it is possible to use the average residual value to select a sample of cosmic muons enriched in the high-energy component, recovering the precision obtainable with high-energy test beams. The operation is not effective if the residual distribution is too broad because the residuals of the track fit are much larger compared to the effect of multiple scattering.

One purpose of this note is to present the method we developed to infer the best value of t_0 for each event to obtain the best precision for the determination of track parameters.

3.3 Simple Straight Line Fit

As already said, neglecting t_0 in the drift time determination yields track parameters with poorer precision. For comparison, in the following we will briefly describe the algorithm and results of a simple straight line fit without t_0.

The first step in any track reconstruction is "pattern-recognition", in which the hits belonging to the same muon track are identified and the left-right ambiguity inherent to any drift chamber is resolved (see the event display plot in Fig. 5 for clarification).

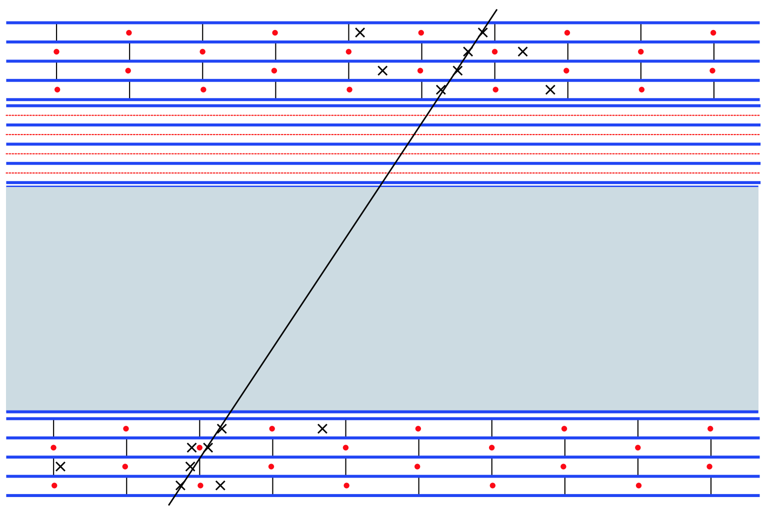

Figure 5: Example of a single event display. The left-right ambiguity of the hits is shown with a cross. Black dots show the position of the wires.

Thanks to the low flux of cosmic rays, the average time separation between consecutive events is 3 orders of magnitude larger than the maximum drift time of ionization electrons in a cell. Therefore for most of the events only 1 track is present, making the pattern recognition a non-critical task. We used the pattern-recognition software developed for the official CMS OO-reconstruction program ORCA [8]. The algorithm was adapted to cosmic-muon reconstruction by simply increasing the measurement error to ≈450 μm to take into account both the t_0 uncertainty and the possible effects of multiple scattering for low-momentum muons. This value is an empirical compromise between the necessity of retaining all good tracks and efficient ghosts rejection. A linear drift space-time relationship inside the cell was assumed with a uniform drift velocity $v_D = 54.7$ μm/ns: as we will explain later, this is the mean of the fitted values obtained with our fitting algorithm. The algorithm loops over all possible hit combinations in each SL independently and in the 2 SL_Φ combined, selecting the hits of the best straight line fit, i.e., the one with the biggest number of points and the lowest χ^2.

A simple straight line fit is therefore used to compute the muon track parameters. The track distance from the wire in cell i is deduced from the drift time ($t_{drift,i}$), assuming linear space-time relationship and using t_{trig} only to estimate t_μ, neglecting the t_0 variation. The residuals are computed as the difference between the hit position and the position inferred from the fit, in the wire plane. Let's define the quantity $\hat{\sigma}^2 = \sum_i res_i^2/NDF$: a simple straight line fit gives the residual distribution shown in Figure 6, in which $\hat{\sigma}^2$ is plotted. The square root of the mean of the $\hat{\sigma}^2$ distribution, let's call it $\sigma^{cell} = \sqrt{<\hat{\sigma}^2>}$, is the best statistical estimate of the resolution of the track coordinate measurements in a single cell, averaged over track angle and impact point. From Figure 6 σ^{cell}=790μm.

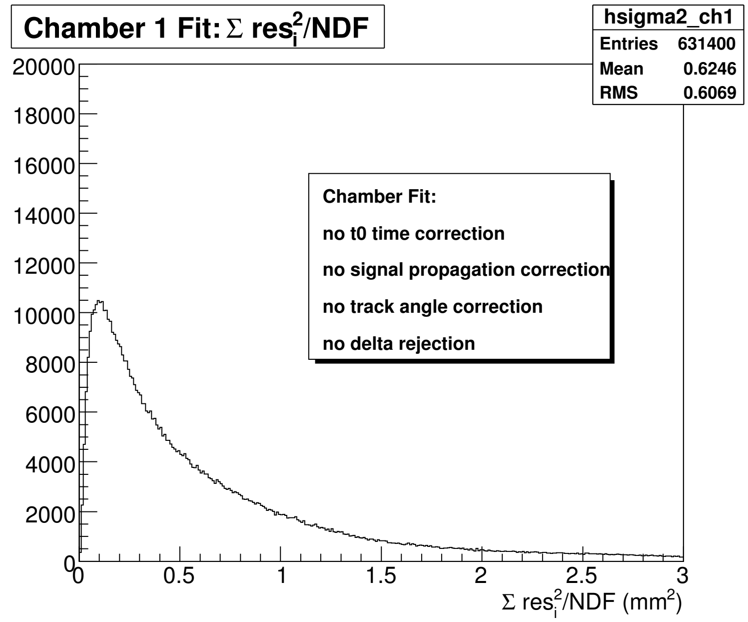

Figure 6: Distribution of $\hat{\sigma}^2$ from simple straight line fit with t_{trig} used as time of passage of the particle.

A very useful quantity to study the drift time measurement precision is the "Mean Time" (MT). To understand the properties of this quantity, consider Figure 7. It shows a track passing through a SL and contained in a semicolumn, the gray region in the figure, composed by 4 half cells located in the same x coordinate interval. The width D of the semicolumn is half the wire pitch. Let d_i be the distances of the track from the wires in the 4 planes, measured in each wire plane. The following geometrical relations hold:

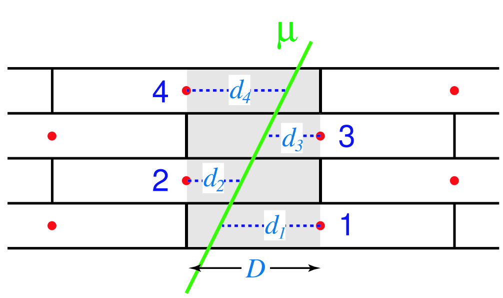

Figure 7: Example of a track completely contained in a semicolumn (the gray area).

$$D = \frac{d_1 + d_3}{2} + d_2 \tag{1}$$

$$D = \frac{d_2 + d_4}{2} + d_3. \tag{2}$$

The relations hold for any angle or position of the track, as long as it is contained in the semicolumn. If the space-time relation is linear, similar equations hold for the drift times:

$$MT_{123} = \frac{t_{drift_1} + t_{drift_3}}{2} + t_{drift_2}. \tag{3}$$

$$MT_{234} = \frac{t_{drift_2} + t_{drift_4}}{2} + t_{drift_3}. \tag{4}$$

where the subscripts 123, and 234, indicate the 3 layers used in the combination. Since the MT value is constant, equal to the time needed to drift across the full semicolumn, its experimental width is directly related to the precision of the drift time measurements.

Figure 8 shows the MT distribution when the drift times are computed neglecting the t_0 correction.

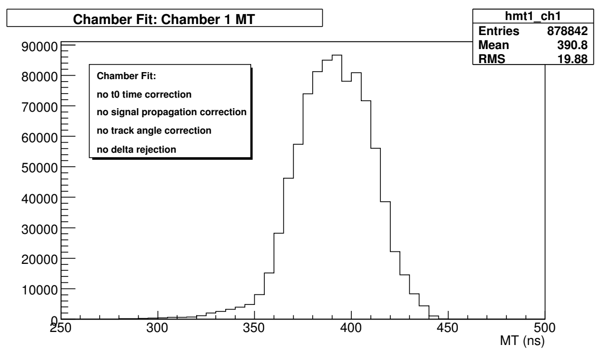

Figure 8: Mean Time distribution when t_{trig} is used as time of passage of the particle on the wire.

The FWHM of the distribution is about 50 ns, as expected from the full width of the expected t_0 distribution, which is about 25 ns. The tail on the left side of the peak is due to δ-ray production, as described in section 3.2. To avoid bias from δ-ray tail, in the following analysis we will fit the MT distribution with a Gaussian function around the peak, and measure the MT average value and resolution from it.

3.4 Straight Line Fit with t_0 estimate

As discussed above, we introduce an unnecessarily large error if we neglect t_0 in the drift time computation. Since any error on $t_{drift,i}$ increases the residuals of the track fit, the idea is to leave t_0 as a free parameter in the track equation and estimate its value minimizing the χ^2 of the fit.

This procedure has already been used to analyze cosmic data [9], [10]. The present note carries forward the previous work, extending it to the simultaneous analysis of all 12 layers of one or several chambers to obtain the best possible determination of t_0 and therefore the best determination of t_μ. The method can be extended to any number of layers. A global fit of all 24 layers (the 2 chambers in sequence) is possible in our setup. In the present note we will focus mainly on the single chamber fit, with the purpose of comparing the results of the 2 chambers. In Section 5 we will present briefly some results of the global fit procedure.

See Appendix 6 for techical details about the fit computation.

3.5 Drift Time Corrections

The distribution of $\hat{\sigma}^2$ for the fit of a single chamber with t_0 estimate, is shown in Figure 9. The Mean Time is shown in Figure 10 as well, computed using the t_0 fitted value.

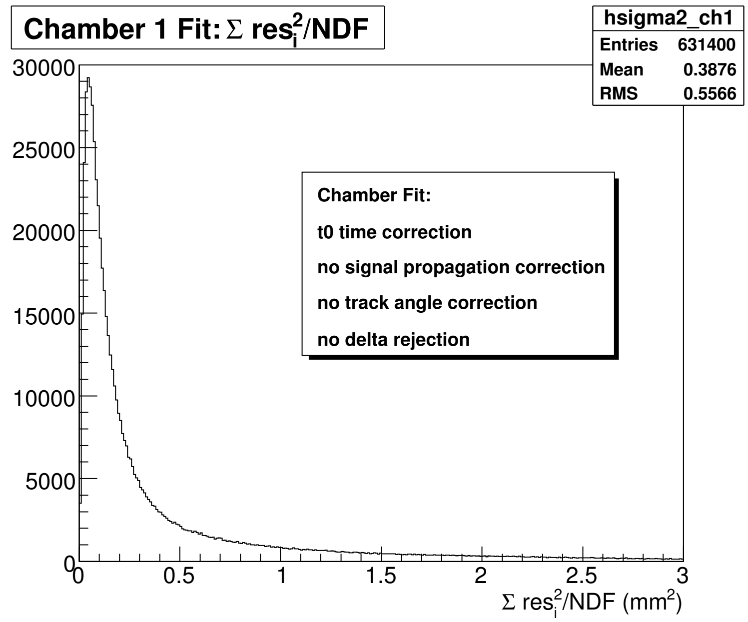

Figure 9: $\hat{\sigma}^2$ from straight line fit with t_0 estimate.

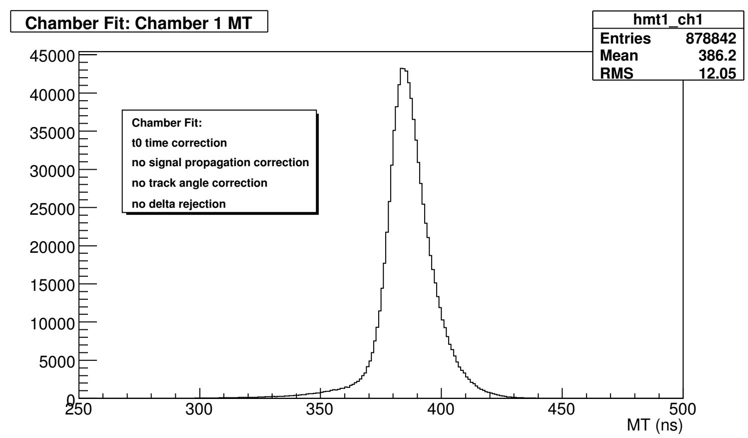

Figure 10: Mean Time for chamber 1 SuperLayers, computed using the t_0 value from the chamber fit.

These figures should be compared with Figures 6 and 8 where the t_0 was not considered in the t_{drift} computation. The hit resolution is improved when t_0 is considered in the fit. However, the tail on the right of $\hat{\sigma}^2$ is longer then expected if a gaussian distribution of the residual is hypothesized. We can identify 2 contributions:

1. Signal propagation along the wire: the muon generates an avalanche around the wire in the vicinity of the intersection between the track and the chamber layer. The electric signal then propagates along the wire to the front-end discriminator. Since the propagation time depends on the impact point, a correction must be applied event by event.

2. Track angle correction: a linear relationship between the drift time and the coordinate of the track in the wire plane is assumed in the fit equations. This assumption is no longer correct for tracks at large angle of

incidence. Due to the cell field shape (see the drift and isochronous lines in Figure 2) and for large angle tracks, the first ionization electrons arriving to the wire make a shorter path than the electrons released near the wire plane. The delay of the latter depends on the angle of the track but also on the muon track distance from the wire. We will assume that a large fraction of this effect, on average, can be fixed with an appropriate drift time shift.

Therefore the correct expression for the drift time should be

$$t_{drift,i} = t_i - t_0 - t_{p,i} + t_{\alpha,i} \tag{5}$$

where
- $t_{p,i}$ is the signal propagation time along the wire from the track crossing point to the end of the wire where the FE is located. It is different in the two Φ and Θ views, but is essentially the same for all the layers in the same view,
- $t_{\alpha,i}$ is the phenomenological correction used to take into account the nonlinearity of the space-time relation for inclined tracks. Again, it is different in the two Φ and Θ views because it depends on the track angle in the plane perpendicular to the wires, but it is the same for all the layers in the same view.

We must correct the drift times in order to make a simultaneous fit over all 12 layers, since both $t_{p,i}$ and $t_{\alpha,i}$ are different in the 2 views. If the fit is performed in one view only, the t_0 parameter obtained (called $t_{0\Phi}$ or $t_{0\Theta}$ in the following) will automatically contain the t_p and t_α corrections, and will be related to the event t_0 correction by $t_{0\Phi} = t_0 + t_{p\Phi} - t_{\alpha\Phi}$ in the Φ view, or $t_{0\Theta} = t_0 + t_{p\Theta} - t_{\alpha\Theta}$ in the Θ view. In conclusion, the best t_0 estimate obtained with the 12-layer fit requires both $t_{p,i}$ and $t_{\alpha,i}$ corrections. In the following subsections the correction evaluation will be outlined.

3.5.1 Signal propagation along the wire

The propagation time along the wire can be measured by studying the MT mean value dependency on the track impact point position. The MT is a sensitive observable because its width is small, and a $t_{drift,i}$ variation Δt produces a MT variation twice as big: $\Delta(MT) = 2 \cdot \Delta t$.

We proceed as follows. A straight line fit through the 8 points of the Φ view is performed, finding the best $t_{0\Phi}$ parameter (the Φ view is chosen due to the larger number of layers). This fitted $t_{0\Phi}$, as discussed before, includes the propagation time along the Φ wires. $t_{0\Phi}$ is then used to compute the Θ drift times for MT_Θ computation.

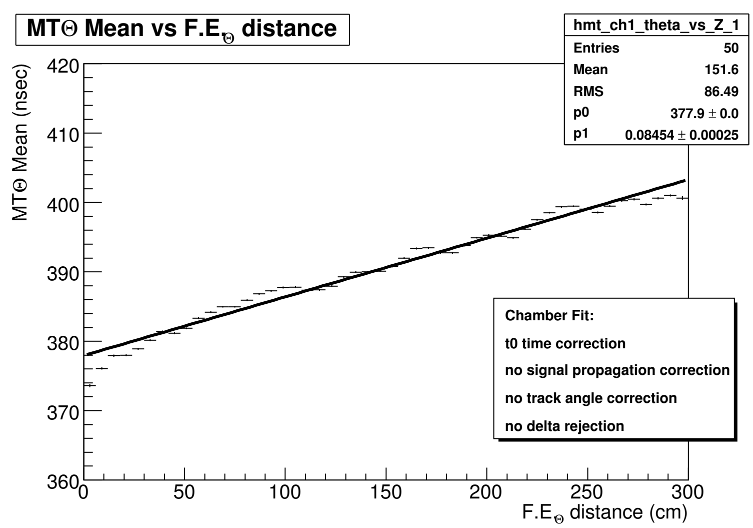

Figure 11: MT_Θ mean value versus distance from the Front End Θ , using $t_{0\Phi}$ as the t_0 value.

Figure 11 shows the MT_Θ mean value versus the distance from the Θ Front End (the mean is computed in small intervals of the distance). Figure 12 shows the same quantity versus the distance from the Φ Front End. Since MT_Θ depends on both distances, the mean value of MT_Θ could be plotted against the difference of the distances from the 2 FEs. In this way a more precise measurement of the propagation velocity can be obtained. Figure 13 gives this last

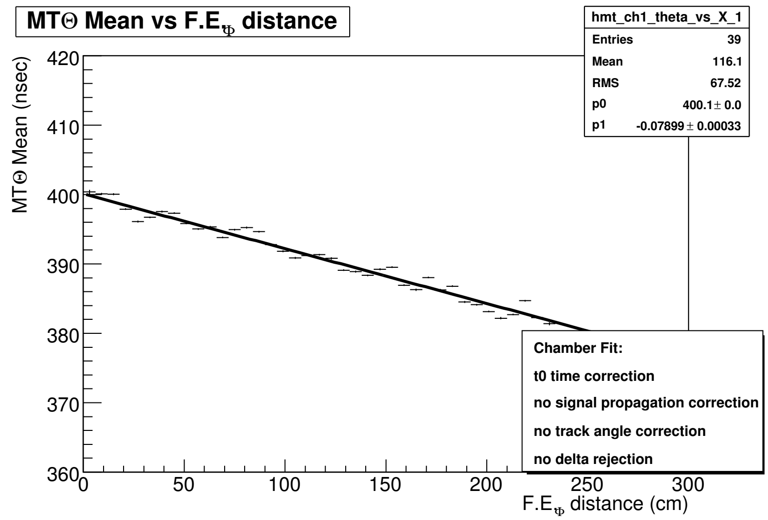

Figure 12: MT_Θ mean value versus distance from the Front End Φ, using $t_{0\Phi}$ as the t_0 value.

correlation. Fitting the plot with a straight line gives a signal propagation velocity of $v_{prop} = (24.0 \pm 0.1)$ cm/ns, where the error is merely statistical. This value is consistent with the one obtained with test bench measurements. The value v_{prop} = 24.0 cm/ns has been used in our analysis.

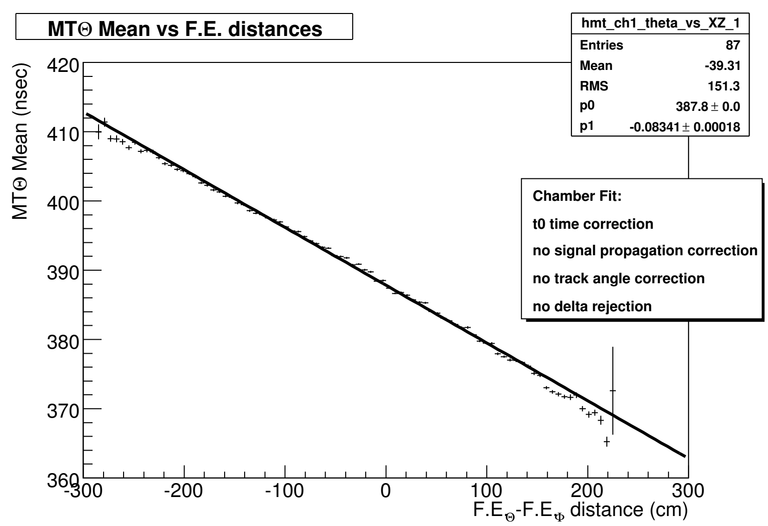

Figure 13: Mean Time Θ versus sum of distances from the Front End Φ and Front End Θ, using $t_{0\Phi}$ as the t_0 value.

3.5.2 Track Angle Correction

In the following analysis the drift times were previously corrected for the propagation time along the wires, according to the results presented in the previous section. The MT_Θ variable will be used to investigate track angle effects.

As in the previous paragraph, a straight line fit through the 8 points of the Φ view alone was performed, and $t_{0\Phi}$ was used to correct the Θ drift times. Then MT_Θ was calculated. Tracks with small angle in the Φ view ($|\Phi| < 0.1$) were selected to isolate the Θ angle dependency, avoiding Φ angle bias in the $t_{0\Phi}$ computation. The mean of the MT_Θ values as a function of Θ is shown in Figure 14. The Mean Time fluctuates in 8 ns range for angles spanning from -25^o up to 25^o. This result is in agreement with the analysis performed previously; see for example [9].

Unfortunately, using the Mean Time restricts the analysis to tracks contained in a semicolumn. This constraint

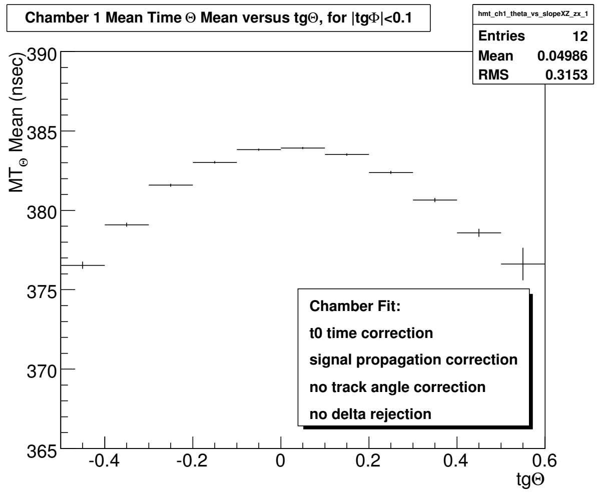

Figure 14: Mean Time Θ versus Θ slope when vertical tracks are selected in the Φ view and using $t_{0\Phi}$ as the t_0 value.

biases the distribution of the impact point and limits the track slope to the range [-0.5, +0.5]. A different method was considered for a full angular range and an unbiased impact point distribution analysis. Two independent track fits were performed in the Θ and Φ views, with independent values of t_0. The best estimates of $t_{0\Phi}$ and $t_{0\Theta}$ was obtained. The dependence of the difference $\Delta t_0 = t_{0\Theta} - t_{0\Phi}$ on the track angle was analysed. Since the propagation time effect was already taken into account, it follows that $\Delta t_0 = (t_0 - t_{\alpha\Theta}) - (t_0 - t_{\alpha\Phi}) = t_{\alpha\Phi} - t_{\alpha\Theta}$.

First, tracks with a small Φ slope were selected, for which $t_{\alpha\Phi}$ is negligible, so that $\Delta t_0 \approx -t_{\alpha\Theta}$. Figure 15 shows how Δt_0 depends on the Θ slope. The shape is almost perfectly parabolic in the full angular range. The same result was obtained by selecting tracks with small Θ and plotting Δt_0 against the Φ slope. Therefore, for all the events and without any angular cut, the difference Δt_0 is expected to depend on the track angles as $\Delta t_0 = -K \cdot \left[(tg\Theta)^2\right] - (tg\Phi)^2$. The linear dependency is shown in Figure 16. A linear fit of the plot gives for K the value $K = (19.79 \pm 0.04)$ ns. This value has been used in the analysis of chamber fit results.

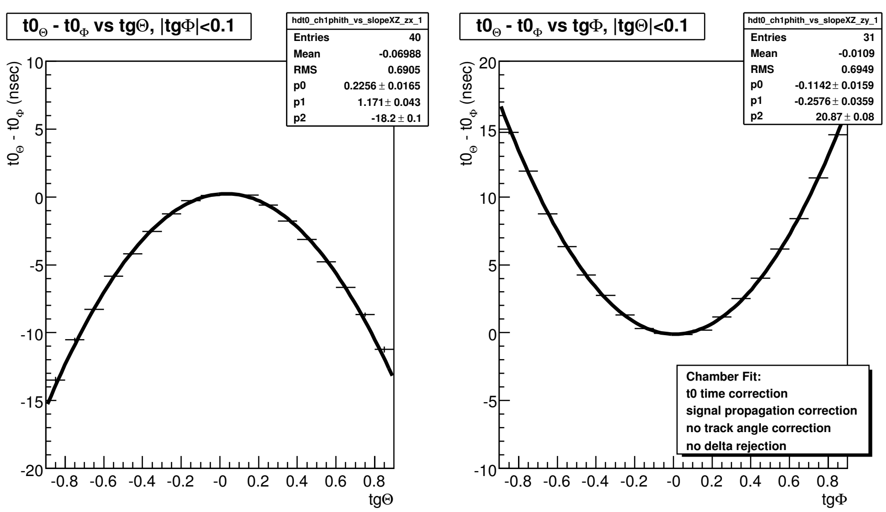

Figure 15: $(t_{0\Theta} - t_{0\Phi})$ versus track slope before angle correction.

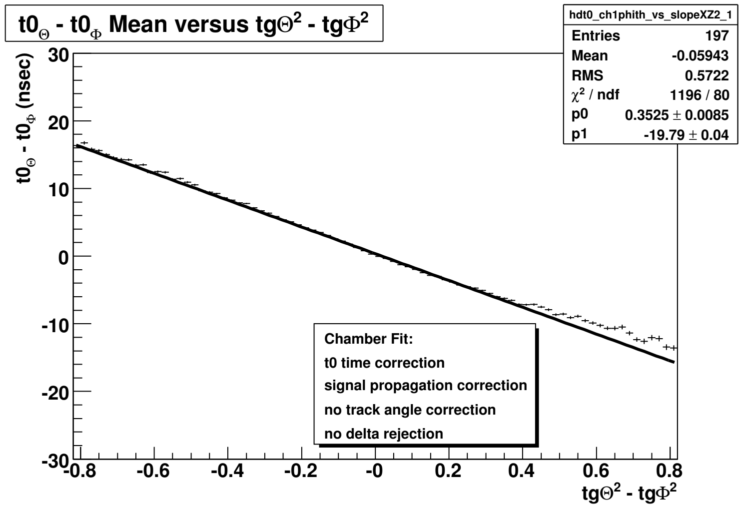

Figure 16: $(t_{0\Theta} - t_{0\Phi})$ versus $\left[tg^2(\Theta) - tg^2(\Phi)\right]$ before angle correction.

4 Analysis of Chamber Fit Results

All corrections discussed so far were applied to the full data sample, i.e., the drift times were corrected for the signal propagation along the wire delay and for nonlinearity of the large angle effect. Preliminary values of the impact coordinates and track angles given by the pattern recognition were used to perform the correction. Afterwards, the tracks were fitted in each of the 2 chambers separately, following the method described in Section 3.1. In this way the t_0 value given by the fit represents the best estimate of the track crossing time for any impact point or angle of incidence of the track.

4.1 t_0 resolution

The main purpose of the fit procedure discussed in this note is to minimize the track parameters errors by obtaining a precise estimate of t_0. To measure the precision obtained, the t_0 estimates of the 2 chambers were compared: the average value of the t_0 difference measures the muon time of flight (t.o.f.) from the upper to the lower chamber. The t.o.f. is expected to vary with the track angle as h/cos(α), where α is the angle of the track with respect to the vertical and h is the distance between the middle planes of the 2 chambers. The t.o.f. variation with the track angle is not affected by systematic uncertainties of the time measurement. Figure 17 gives the average value of the t_0 difference in small intervals of the angle α plotted against 1/cos(α). The expected linear dependence is evident, and the size of the variation is congruent to the relative distance of the 2 chambers. From the figure the slope is 1.757 ns = h/c, from which h = 52 cm, in agreement with the chambers position in our stand ($\approx$50 cm). The intercept fails to give the expected 1.5 ns value. This can be explained considering that the test pulse distribution system in the two chambers can produce a small difference of the order of 0.5 ns in their absolute time origin.

A comparison between the t_0 values of the 2 chambers was performed to measure their precision. The difference of the two t_0s was corrected taking into account the angle dependency shown in Figure 17 and it is plotted in the histogram of Figure 18. The r.m.s. of the distribution is equal to 3.4 ns, from which a t_0 precision of 2.4 ns for the single chamber fit is deduced. Neglecting the tails, the histogram can be fitted with a gaussian function with 2.6 ns width, corresponding to a chamber time resolution of 1.8 ns.

The precision of the t_0 determination gives a narrow distribution of the Mean Time variable, as observed in Figure 19.

4.2 Residuals

The distribution of $\hat{\sigma^2}$ when all corrections have been applied is shown in Figure 20. The best estimation of the chamber resolution is $\approx$334 μm, much lower than the value of 623 μm inferred from Figure 9, but still larger than the $\approx$200 μm observed with test beam data.

We can identify 2 possible sources for this discrepancy:

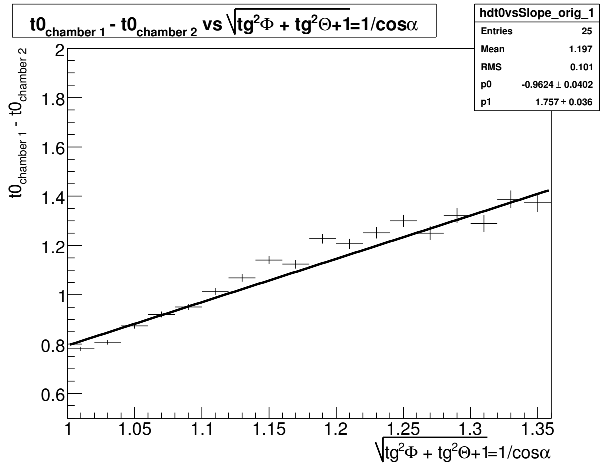

Figure 17: t_0 difference between chambers 1 and 2 versus 1/cos(α).

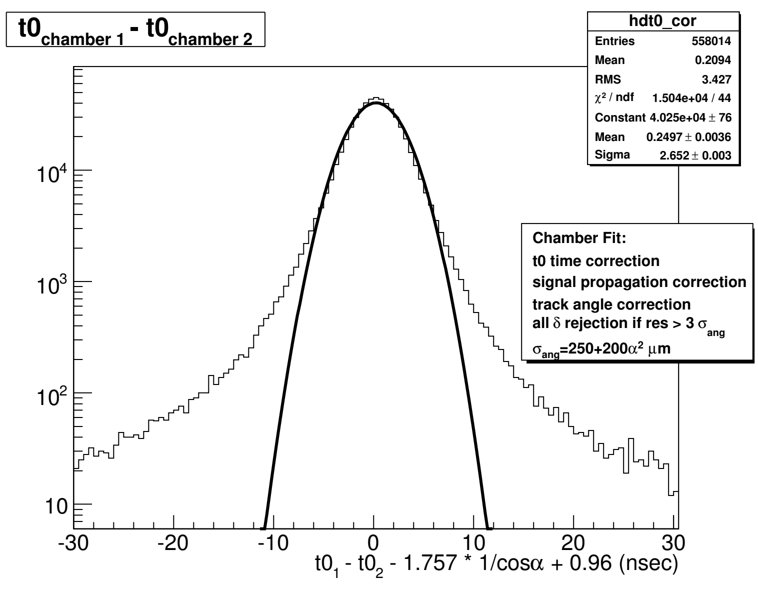

Figure 18: t_0 difference between chambers 1 and 2, all corrections applied.

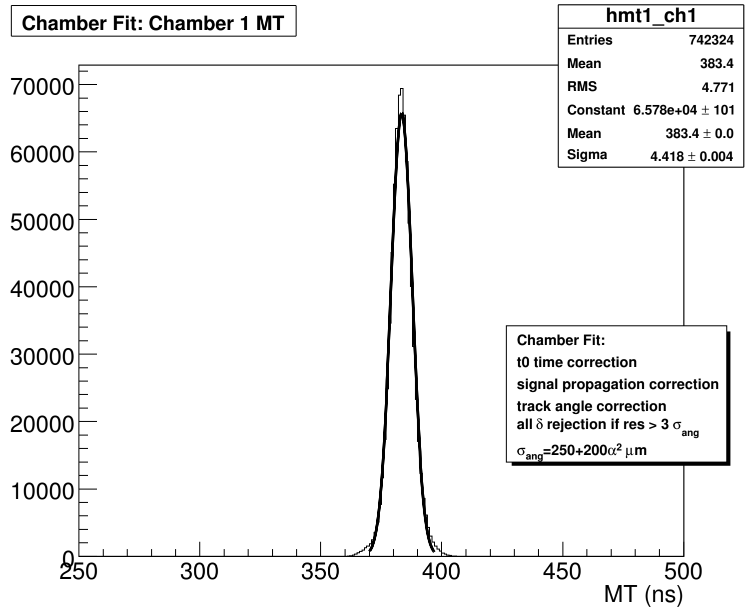

Figure 19: Mean Time Φ, all corrections applied.

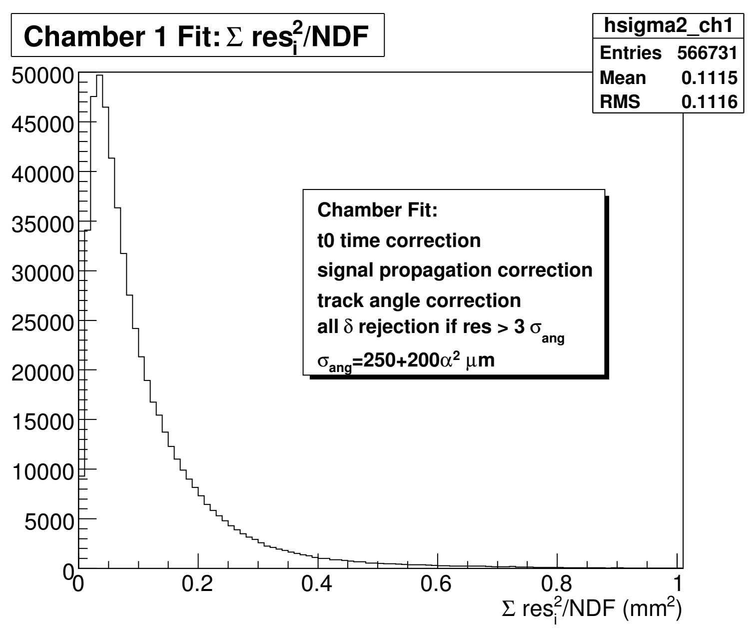

Figure 20: $\hat{\sigma}^2$ from the straight line fit with all corrections applied.

- The cosmic muon momentum spectrum has a large component of low momentum particles, down to few hundred MeV. In this range multiple scattering in the chamber material can have a sizeable effect.
- The angular distribution of cosmic-ray data is much broader than what is usually considered when taking data in test beams. As discussed in Section 3.5.2, the linearity between drift time and distance of the track crossing point from the closest wire fails for large angle tracks. Therefore we expect larger residuals for large angle tracks.

These hypotheses will be analyzed in the following sections.

4.2.1 Residuals and Muon Momentum

High momentum track residuals are essentially due to measurement errors. On the other hand, low momentum track residuals are expected to be large, due to increased multiple scattering of the particle through the chamber material. Therefore, a correlation between the fit residuals in the 2 chambers is expected, and it should be larger for the low momentum component of the spectrum. This correlation is indeed observed in Figure 21 where the distributions of $\hat{\sigma}^2 = \Sigma res_i^2/NDF$ in one chamber are shown for different intervals of the χ^2 value in the other chamber.

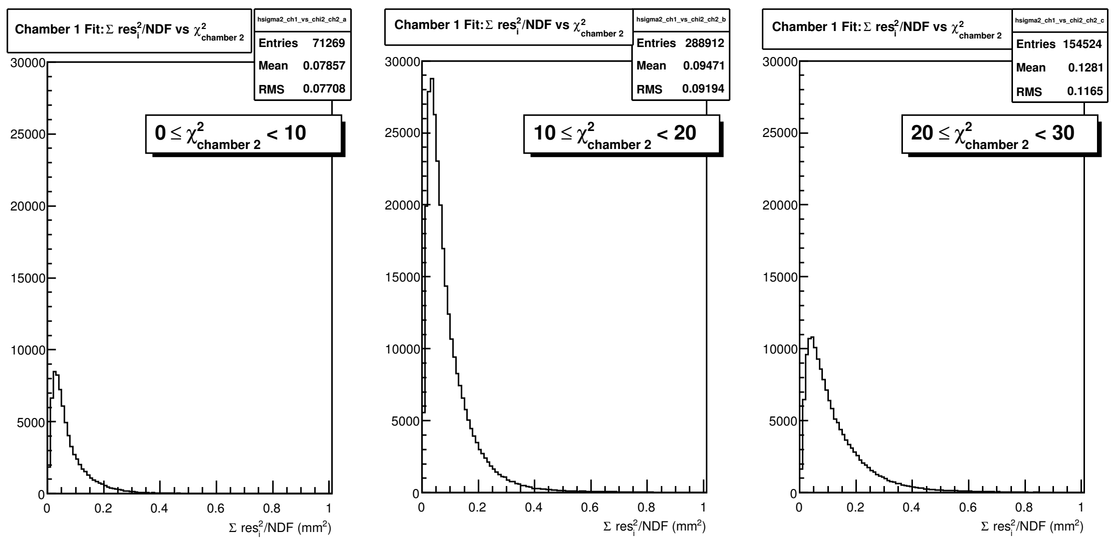

Figure 21: $\hat{\sigma}^2$ distribution in chamber 1 for different χ^2 ranges of the fit in chamber 2.

Figure 22 shows the $\hat{\sigma}^2$ distribution for tracks with small Φ and Θ angles ($|\Phi| < 0.2$, $|\Theta| < 0.2$) and small residuals in chamber 2 ($\chi^2 < 15$ of chamber 2). The estimated value of the standard deviation of the residuals is 254 μm, not far from test beam data results [11].

4.2.2 Residuals versus Angle

Figure 23 shows the distribution of residuals in the Φ view for different Φ-angle slices. A clear correlation of the width of the distribution with the angle is observed.

To measure the correlation, the data were divided in small Φ slices and the chamber resolution σ_{cell} was computed in each Φ bin. The resolution value is plotted with red stars in Figure 24 versus the central value of the Φ interval. An approximate quadratic correlation is displayed. The observed Φ dependence of resolution can be due both to multiple scattering, since at large angles the particle traverses a bigger thickness of material, and to nonlinear effects of the space-drift time relation. A Monte Carlo simulation is also shown in Figure 24 with black dots. In the Monte Carlo simulation, the momentum spectrum of the cosmic muons and the materials of the chamber structure have been taken into account, but the space-drift time relation has been assumed to be linear at all angles. The increase of the residuals, due to the contribution of the multiple scattering, appears to be small. The effect of non linearity could be corrected in principle by measuring the exact space-drift time relation as a function of the angle. This further step is outside the scope of this note and will be the subject of a forthcoming work.

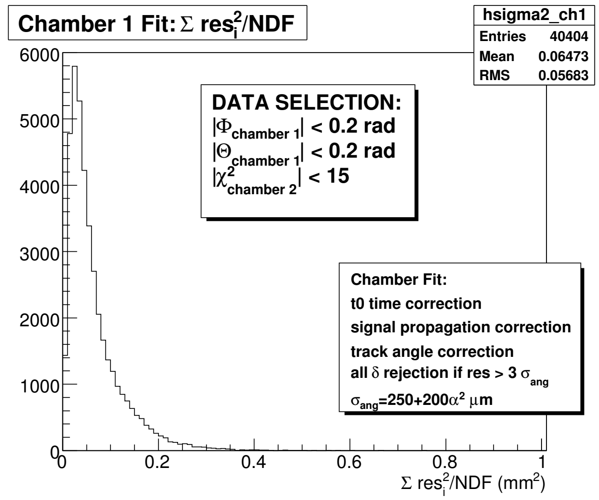

Figure 22: $\hat{\sigma}^2$ distribution of chamber 1 fit for small Φ and Θ angles and low χ^2 in chamber 2.

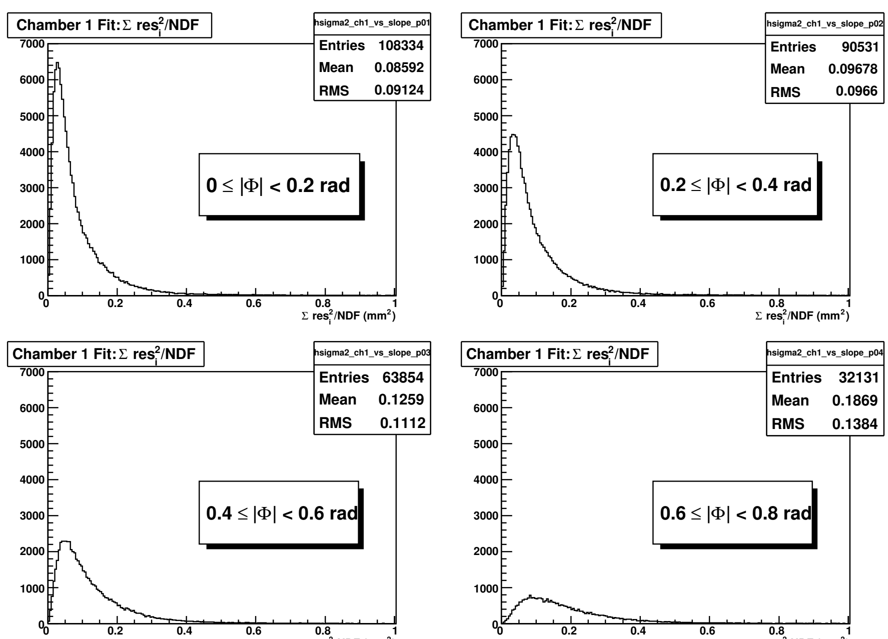

Figure 23: $\hat{\sigma}^2$ distribution in chamber 1, for different Φ ranges.

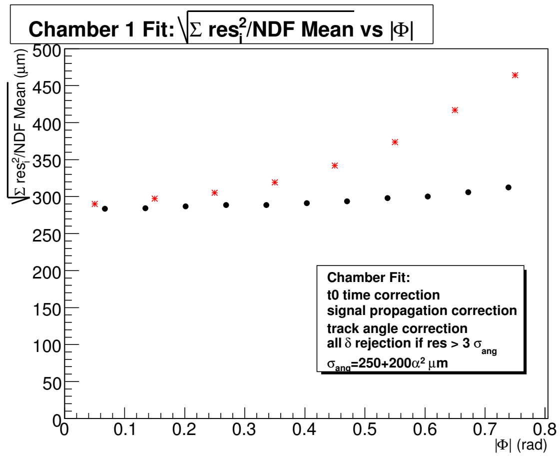

Figure 24: Resolution σ_{cell} in the Φ view, versus Φ angle, for cosmic-ray data (red stars), compared with Monte Carlo simulation (black dots).

4.3 Track Slope Measurement Precision

A comparison between the slopes of the 2 chambers measured in the Φ and Θ views allows the measurement of the precision with which the slopes are measured, given that the 2 chambers are well aligned. The Φ slope difference is shown in Figure 25. The r.m.s. value of the histogram, in the range -40 to $+40$ mrad, is 9 mrad, corresponding to a Φ slope precision of about 6 mrad, much larger than the resolution measured in high energy test beam data [11]. This large value is due to the low momentum component of the cosmic ray spectrum, extending to values as low as few hundred MeV/c. For such muons multiple scattering can modify the direction of the particle by an angle bigger than the measurement resolution. The Monte Carlo simulation quoted in the previous paragraph is in agreement with this result, as it is shown in Figure 25, were the Monte Carlo distribution is shown as a gray area.

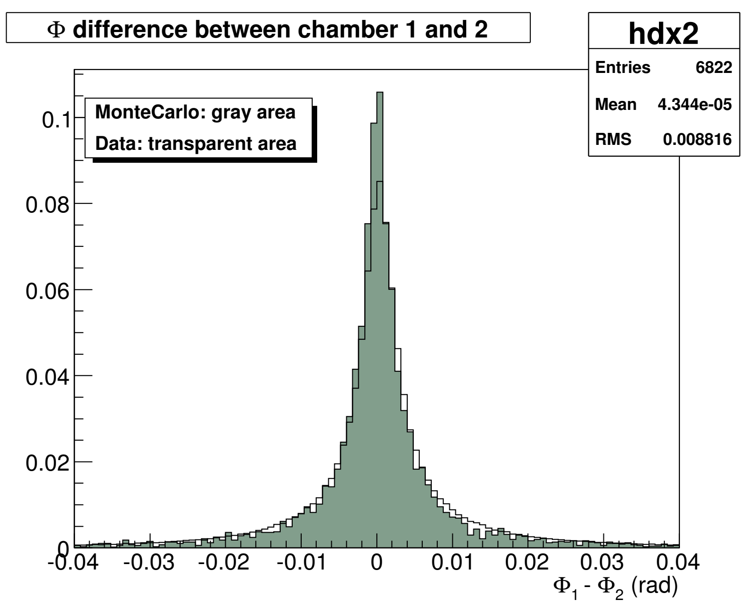

Figure 25: Φ Slope difference between chambers 1 and 2, compared with Monte Carlo simulation.

We can recover the Φ slope precision using the χ^2 of 1 chamber fit to cut the low momentum component of the cosmic-ray spectrum. The correlation is clear from Figure 26, were the Φ slope difference histograms are shown for different intervals of the χ^2 of chamber 2.

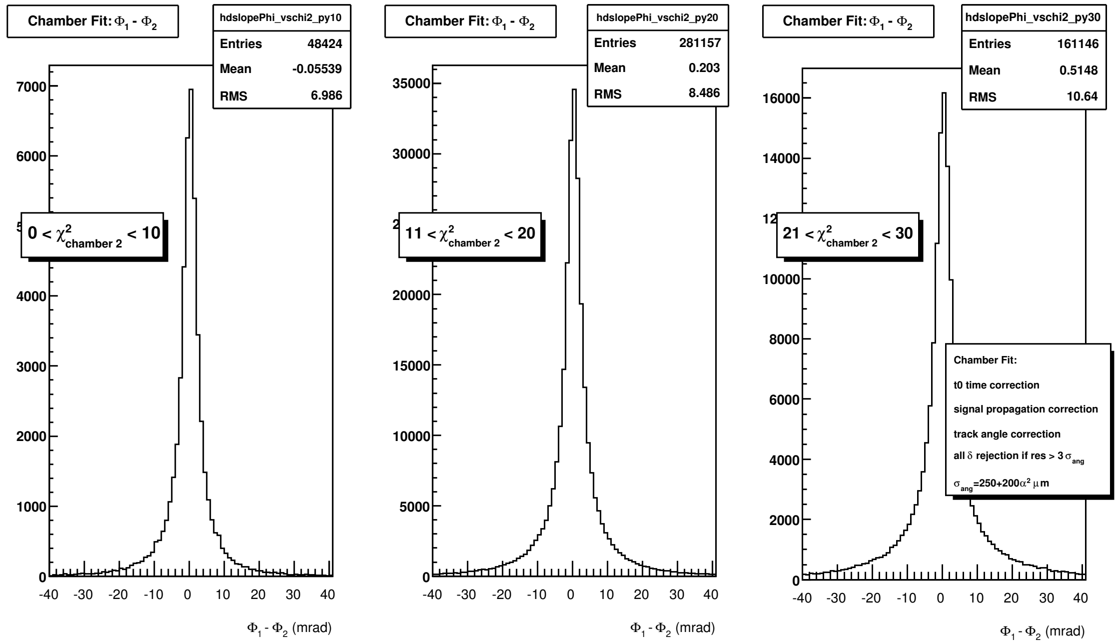

Figure 26: Φ Slope difference for different χ^2 of chamber 2 slices.

The resolution of the Θ slope, shown in in Figure 27, is large enough to cover the effect of multiple scattering.

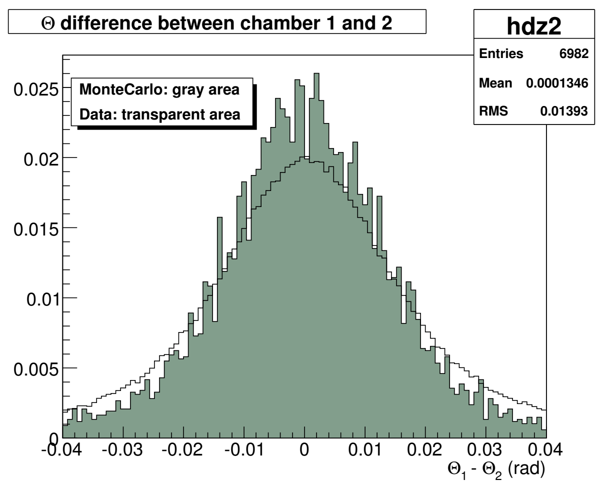

Figure 27: Θ Slope difference between chambers 1 and 2, compared with Monte Carlo simulation.

The Φ view fitted slope is much more precise than the one in the Θ view mostly because of the large separation between the two SL_Φs. Thanks to this large separation the slope measurement is less affected by systematic errors too, e.g., the ones deriving from the assumption that the space-drift time relationship is linear. Therefore, it is interesting to compare the measurement of the Φ angle obtained with 1 single SL_Φ (ϕ_1 or ϕ_2 in the following) and the one obtained with both SLs (ϕ_{12}). With this intent, data were divided in bins of ϕ_{12}, and the $\Delta\phi = \phi_{12} - \phi_1$ distribution of each sample was fitted with a gaussian function. In this way systematics effects, if any, could be seen. Figure 28 shows the mean value and the width of the gaussian function plotted versus the central value of the ϕ_{12} interval for chamber 1. No systematic effect is visible, apart from a slight increase of the width for the larger angles. The small fluctuations of the mean value around 0 are compatible with the construction alignement precision of the layers inside a SL (better than 100 μm). This result guarantees that the angle measurement in the Θ view, obtained with only 1 superlayer, is not affected by significant systematic biases.

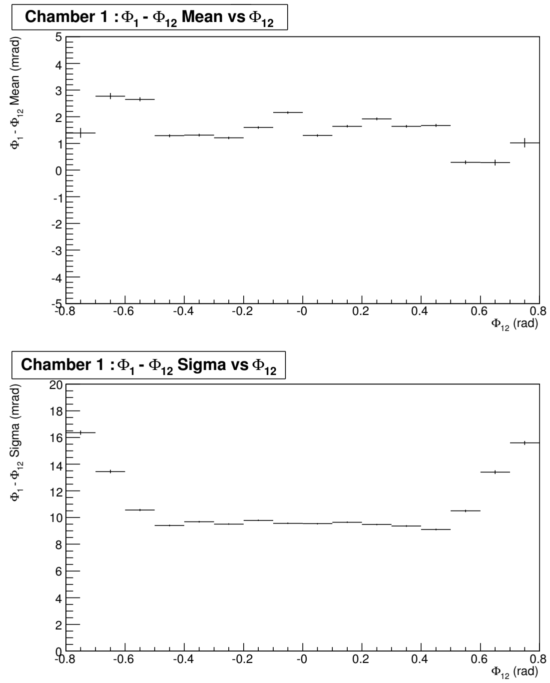

Figure 28: Difference $\Delta\Phi = \phi_{12} - \phi_1$ plotted against the slope (see text for the meaning of symbols). Top: Mean value of $\Delta\Phi$ versus Φ. Bottom: Sigma of $\Delta\Phi$ versus Φ.

The same analysis was repeated for chamber 2. After having increased the distance between the two SL_Φ by 1.5 mm with respect to the nominal value, the expected absence of bias could be observed. We verified *a posteriori* that the honeycomb panel of this chamber had been built outside tolerance and the thickness was 1.5 mm larger than the design value. This result shows that cosmic-ray track analysis could be a powerful tool to spot and correct construction anomalies in the chambers.

4.4 Fit of the drift velocity

As already said, all the results presented were obtained with a fixed drift velocity value ($v_D = 54.7$ μm/ns). On the same data sample, a fit with the drift velocity left as free parameter was also performed. Figure 29 shows the value of the velocity given by the fit in each of the 2 chambers. The average values in the 2 chambers are very close and consistent with the value we used. The r.m.s. of the distribution is $\approx$4%. This is the precision with which a single track can measure the effective drift velocity, assuming that it is the same in all layers.

5 Global Fit Results

A simultaneous fit to both chambers is expected to reduce the error on t_0 by a factor $\sqrt{2}$, i.e., from 2.4 ns to about 1.7 ns.

We expect to observe the presence of such a small effect (from 130 μm to 90 μm in space) only in events with the best resolution. Figure 30 shows the Φ slope difference histograms for different intervals of χ^2 of chamber 2. This figure should be compared with Figure 26, where the same quantity was plotted, fitting the 2 chambers independently. An improvement is present, more important for low χ^2. Unfortunally, we cannot say if the global fit improves the precision of the angle measurements, or if the decrease of the t_0 error contribution on the residuals improves the momentum selection operated by the χ^2 cut. The global fit procedure is expected to give better results when more than 2 chambers are considered.

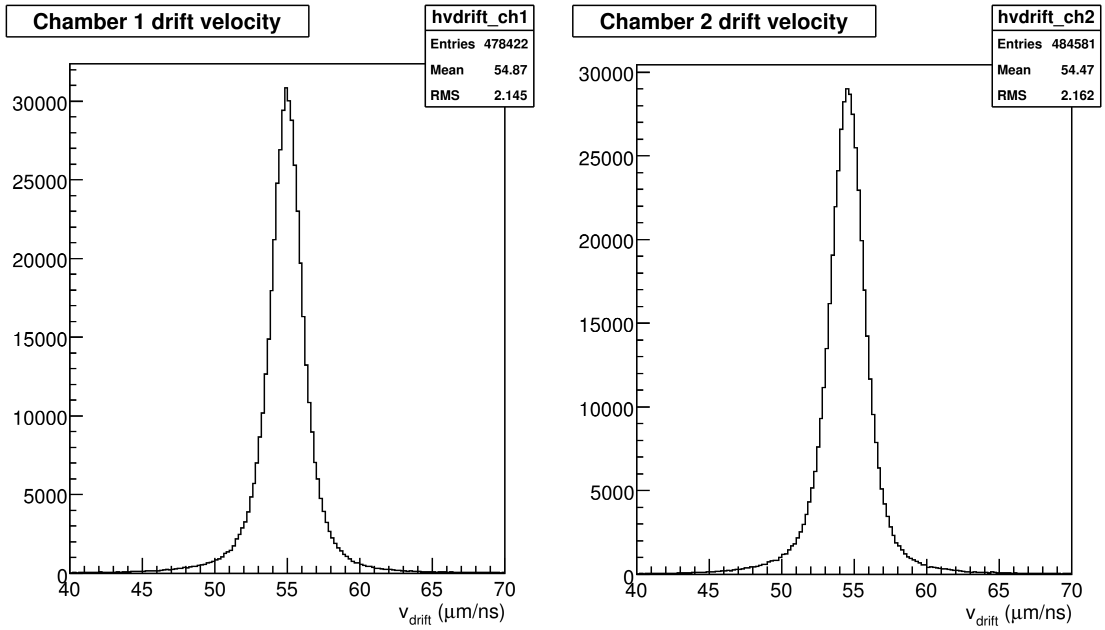

Figure 29: Fitted drift velocity in the chambers.

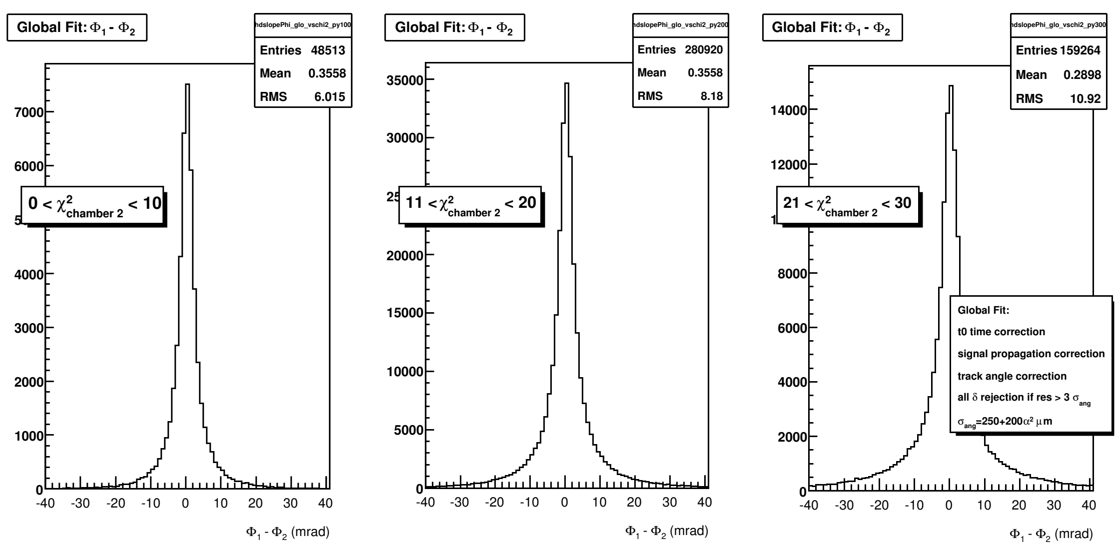

Figure 30: Slope difference for different chamber 2 χ^2 slices.

6 Conclusions

Two MB3 chambers assembled in the I.N.F.N. production center at LNL were extensively studied using a cosmic-ray test facility that was set up in the laboratory to test the chamber behaviour. In our analysis, we developed and verified a fitting procedure to find the best timing precision in the absence of external timing devices.

A timing precision from a single chamber of 2.4 ns was observed. Selecting tracks with low χ^2 in a chamber allows the selection of a sample of muons with high enough momentum that the resolution of the other chamber can be measured with a precision close to the one measured in high energy test beams, with a uniform illumination of the chamber and a large angular spread of the particles crossing the chamber.

A Single Chamber Fit

The trajectory of the particle is described by 2 straight lines in Φ and Θ views. The points associated to a track are identified by the coordinates x_i, y_i, in each layer i, where the x coordinate is in the wire plane and orthogonal to the wires, and y is orthogonal to the wire planes. The y_i coordinate is already assumed known from the nominal geometry of the chamber. The x_i coordinate depends on the drift time $t_{drift,i}$ and on the drift velocity v_D. The drift velocity could be left as a free parameter in the track equation and its value and uncertainty estimated minimizing the χ^2 of the fit too (see comment below). Let's define $t_i = t_{TDC,i} - t_{trig}$, where $t_{TDC,i}$ is the raw time read from the TDC channel of wire i, corrected using test pulse information. Being $t_\mu = t_{trig} + t_0$, we have $t_{drift,i} = t_{TDC,i} - t_\mu = t_i - t_0$.

We will assume a linear dependence between drift time and muon coordinate in the wire plane, given by the expression:

$$x_i = f_i + \epsilon_i v_D t_{drift,i} = f_i + \epsilon_i v_D (t_i - t_0) = f_i + \epsilon_i v_D t_i - \epsilon_i x_0 \tag{6}$$

where:

- f_i is the nominal x coordinate of the wire where the signal was collected. The chamber construction procedure guarantees that the actual wire position differs from the nominal one by at most 100 μm;
- ϵ_i value is +1 or -1, depending on which side with respect to the wire the track is; ϵ_i is assumed to be known from the preliminary pattern recognition algorithm;
- $x_0 = v_D t_0$. The use of the variable x_0 in place of t_0 simplifies the fit equations.

In the following equations we use different indexes for the layers of the Φ and Θ views:

- i index is used for the 8 Φ layers. The straight line has equation $x_i = my_i + a$. The angular coefficient m is 0 for tracks perpendicular to the chamber.
- j index is used for the 4 Θ layers. The line is: $x_j = ny_j + b$.

The χ^2 function to be minimized to find the best lines interpolating the points is:

$$\chi^2 = \sum_i w_i [x_i - (my_i + a)]^2 + \sum_j w_j [x_j - (ny_j + b)]^2 \tag{7}$$

where $w_i = 1/\sigma_i^2$. The error σ_i should include both the measurement error and the error coming from multiple scattering, if known. In the analysis of this note, since we do not have information on the muon momentum, the multiple scattering contribution cannot be considered on an event by event basis.

Making x_i and x_j dependence from v_D and x_0 explicit, we have:

$$\chi^2 = \sum_i w_i [f_i + \epsilon_i v_D t_i - \epsilon_i x_0 - my_i - a)]^2 + \sum_j w_j [f_j + \epsilon_j v_D t_j - \epsilon_j x_0 - ny_j - b)]^2 \tag{8}$$

The variables to be determined by minimizing the χ^2 function are the slopes m, n, the intercepts a, b in the Φ and Θ views, the variable x_0 connected to t_0 and the drift velocity v_D.
The system to be solved is $M\overrightarrow{v} = \overrightarrow{C}$, where the matrix M is:

$$M = \left\| \begin{array}{cccccc} S^i_{yy} & S^i_y & 0 & 0 & S^i_{\epsilon y} & -S^i_{\epsilon t y} \\ S^i_y & S^i & 0 & 0 & S^i_\epsilon & -S^i_{\epsilon t} \\ 0 & 0 & S^j_{yy} & S^j_y & S^j_{\epsilon y} & -S^j_{\epsilon t y} \\ 0 & 0 & S^j_y & S^j & S^j_\epsilon & -S^j_{\epsilon t} \\ S^i_{\epsilon y} & S^i_\epsilon & S^j_{\epsilon y} & S^j_\epsilon & S^{i+j}_{\epsilon\epsilon} & -S^{i+j}_{\epsilon\epsilon t} \\ S^i_{\epsilon y t} & S^i_{\epsilon t} & S^j_{\epsilon y t} & S^j_{\epsilon t} & S^{i+j}_{\epsilon\epsilon t} & -S^{i+j}_{\epsilon\epsilon t t} \end{array} \right\| .$$

and

$$
\begin{aligned}
\overrightarrow{v} &= (m, \quad a, \quad n, \quad b, \quad x_0, \quad v_D) \\
\overrightarrow{C} &= (S^i_{fy}, \quad S^i_f, \quad S^j_{fy}, \quad S^j_f, \quad S^{i+j}_{f\epsilon}, \quad S^{i+j}_{f\epsilon t})
\end{aligned}
$$

The symbols S^i_{pqr} indicate the sum $\sum_i w_i p_i q_i r_i$, e.g. $S^i_{\epsilon y} = \sum_i w_i \epsilon_i y_i$ and $S^i = \sum_i w_i$.

In this system the drift velocity is left as a free parameter. However, being v_D the same for all the particles, more precise results can be obtained fixing it to a value determined independently. The modifications of the above equations to use a fixed v_D are straightforward. Except when explicitly quoted, the results shown in the following have been obtained using a fixed value of $v_D = 54.7$ μm/ns.

B Two Chambers Global Fit

As a reference, we give here the equations used in the global fit. An additional couple of indexes for the second chamber Φ and Θ views is introduced:

- k index is used for the 8 planes of chamber 2 SL_Φ. The straight line has equation $x_k = py_k + c$.
- l index is used for the 4 planes of chamber 2 SL_Θ. The line is: $x_l = qy_l + d$.

The χ^2 function, with v_D and x_0 explicit dependence, this time is:

$$
\begin{aligned}
\chi^2 = \sum_i w_i [f_i + \epsilon_i v_D t_i - \epsilon_i z_0 - m y_i - a)]^2 + \sum_j w_j [f_j + \epsilon_j v_D t_j - \epsilon_j z_0 - n y_j - b)]^2 + \\
\sum_k w_k [f_k + \epsilon_k v_D t_k - \epsilon_k z_0 - p y_k - c)]^2 + \sum_l w_l [f_l + \epsilon_l v_D t_l - \epsilon_l z_0 - q y_l - d)]^2
\end{aligned}
\tag{9}
$$

We have to find solutions for $M\overrightarrow{v} = \overrightarrow{C}$, were:

$$
M = \left\| \begin{array}{cccccccccc}
S^i_{yy} & S^i_y & 0 & 0 & 0 & 0 & 0 & 0 & S^i_{\epsilon y} & -S^i_{\epsilon ty} \\
S^i_y & S^i & 0 & 0 & 0 & 0 & 0 & 0 & S^i_\epsilon & -S^i_{\epsilon t} \\
0 & 0 & S^j_{yy} & S^j_y & 0 & 0 & 0 & 0 & S^j_{\epsilon y} & -S^j_{\epsilon ty} \\
0 & 0 & S^j_y & S^j & 0 & 0 & 0 & 0 & S^j_\epsilon & -S^j_{\epsilon t} \\
0 & 0 & 0 & 0 & S^k_{yy} & S^k_y & 0 & 0 & S^k_{\epsilon y} & -S^k_{\epsilon ty} \\
0 & 0 & 0 & 0 & S^k_y & S^k & 0 & 0 & S^k_\epsilon & -S^k_{\epsilon t} \\
0 & 0 & 0 & 0 & 0 & 0 & S^l_{yy} & S^l_y & S^l_{\epsilon y} & -S^l_{\epsilon ty} \\
0 & 0 & 0 & 0 & 0 & 0 & S^l_y & S^l & S^l_\epsilon & -S^l_{\epsilon t} \\
S^i_{\epsilon y} & S^i_\epsilon & S^j_{\epsilon y} & S^j_\epsilon & S^k_{\epsilon y} & S^k_\epsilon & S^l_{\epsilon y} & S^l_\epsilon & S^{i+j+k+l}_{\epsilon\epsilon} & -S^{i+j+k+l}_{\epsilon\epsilon t} \\
S^i_{\epsilon yt} & S^i_{\epsilon t} & S^j_{\epsilon yt} & S^j_{\epsilon t} & S^k_{\epsilon yt} & S^k_{\epsilon t} & S^l_{\epsilon yt} & S^l_{\epsilon t} & S^{i+j+k+l}_{\epsilon\epsilon t} & -S^{i+j+k+l}_{\epsilon\epsilon tt}
\end{array} \right\| .
$$

and

$$
\begin{aligned}
\overrightarrow{v} &= (m, \quad a, \quad n, \quad b, \quad p, \quad c, \quad q, \quad d, \quad x_0, \quad v_D) \\
\overrightarrow{C} &= (S^i_{fy}, \quad S^i_f, \quad S^j_{fy}, \quad S^j_f, \quad S^k_{fy}, \quad S^k_f, \quad S^l_{fy}, \quad S^l_f, \quad S^{i+j+k+l}_{f\epsilon}, \quad S^{i+j+k+l}_{f\epsilon t})
\end{aligned}
$$

References

[1] *"The CMS Muon Project, CMS Technical Design Report"*, CERN/LHCC 97-32, CMS TDR, December 1997.

[2] *M. Aguilar-Benitez et al., "Construction and test of the final CMS Barrel Drift Tube Muon Chamber prototype"*, Nucl. Instrum. Meth. A **480** (2002) 658.

[3] R. Veenhof, *"GARFIELD. Simulation of gaseous detectors"*, Users Guide v.8.01, CERN Writeups, Ref. W5050 (2005).

[4] M. Cavicchi, F. Gonella, I. Lippi, P. Guaita, M. Pegoraro, E. Torassa, *“Properties and Performances of a Front-end ASIC Prototype for the Readout of the CMS Barrel Muon Drift Tubes Chambers”*, CMS Note 1999/033.

[5] CMS Collaboration, *“Level-1 Trigger Technical Design Report”*, CERN LHCC 2000-038.

[6] C. Fernandez Bedoya, J. Marin, J. C. Oller, C. Willmott, *“Electronics For The Cms Muon Drift Tube Chambers: The Read-Out Minicrate”*, IEEE Trans. Nucl. Sci. **52** (2005) 944.

[7] M. Benettoni *et al.*, *“Performance of the drift tubes for the barrel muon chambers of the CMS detector at LHC”*, Nucl. Instrum. Meth. A **410** (1998) 133.

[8] *The Object Reconstruction for CMS Analysis program (ORCA)*, http://cmsdoc.cern.ch/orca/.

[9] F.R. Cavallo et al., *“Test of CMS Muon Barrel Drift Chambers with Cosmic Rays”*, CMS Note 2003/017.

[10] M.Benettoni et al., *“Study of the Internal Alignment of the CMS Muon Barrel Drift Chambers using Cosmic Rays Tracks”*, CMS Note 2004/001.

[11] C. Albajar *et al.*, *“Test beam analysis of the first CMS drift tube muon chamber”*, Nucl. Instrum. Meth. A **525** (2004) 465–484.